

Advancements in mathematical modeling and numerical simulation: Immersed boundary method for Navier-Stokes equations applied to stationary and rotating isothermal cylinders

Avanços em modelagem matemática e simulação numérica: Método de fronteira imersa para equações de Navier-Stokes aplicadas a cilindros isotérmicos estacionários e rotativos

Article Info:

Article history: Received 2024-02-06 / Accepted 2024-06-25 / Available online 2024-07-01

doi: 10.18540/jcecv110iss8pp18894



Rômulo Damasclin Chaves dos Santos

ORCID: <https://orcid.org/0000-0002-9482-1998>

Department of Physics, Technological Institute of Aeronautics, São Paulo, Brazil

E-mail: romulosantos@ita.br

Jorge Henrique de Oliveira Sales

ORCID: <https://orcid.org/0000-0003-1992-3748>

State University of Santa Cruz – Department of Exact Sciences, Ilhéus, Bahia, Brazil

E-mail: jhosales@uesc.br

Abstract

This study investigates the growing scientific and industrial interest in the dynamics of fluids around bodies, with a particular focus on thermal fluctuations. These phenomena are prevalent in various scenarios, such as oil extraction platforms, power transmission lines, and fluid-structure interactions, necessitating a comprehensive understanding of vortex generation, heat transfer, and fluid dynamic forces. We employ the Immersed Boundary Method (IBM) to simulate two-dimensional, incompressible flows around stationary and rotating heated (isothermal) cylinders. Using a computational framework developed in C/C++, we analyze the effects of variations in cylinder rotation rates on flow dynamics and thermal distributions. This study involves multiple simulations to evaluate the stability of the method and extract relevant parameters, including drag, lift coefficients and Nusselt numbers, along with velocity, pressure, vorticity, and temperature fields. Through systematic comparison with existing literature, we aim to validate our findings and contribute to the continuous improvement of numerical accuracy in this domain. By elucidating these complex phenomena, our research aims to provide valuable insights for practical applications in industrial and engineering contexts. The objective of this work is to analyze the combination of heat transfer phenomena with rotation in isothermal cylinders and their thermofluid-structure interaction. To achieve this, a low computational cost C/C++ code (in terms of memory and computational resources) was developed. Furthermore, numerical simulations indicated that with an increase in the Reynolds number, there is an increase in the drag coefficient, highlighting the significant influence of the pressure distribution downstream of the cylinder. This pressure distribution is strongly affected by vortex formation and detachment, thereby validating the methodology.

Keywords: Immersed Boundary Method, Isothermal Rotating Cylinder, Numerical Simulation, Incompressible Newtonian Flow.

Resumo

Este estudo investiga o crescente interesse científico e industrial na dinâmica dos fluidos ao redor dos corpos, com foco particular nas flutuações térmicas. Esses fenômenos são predominantes em vários cenários, como plataformas de extração de petróleo, linhas de transmissão de energia e interações fluido-estrutura, necessitando de uma compreensão abrangente da geração de vórtices, transferência de calor e forças dinâmicas de fluidos. Empregamos o Método de Fronteira Imersa (IBM) para simular fluxos bidimensionais e incompressíveis em torno de cilindros aquecidos (isotérmicos) estacionários e rotativos. Utilizando uma estrutura computacional desenvolvida em C/C++, analisamos os efeitos das variações nas taxas de rotação dos cilindros na dinâmica do fluxo e nas distribuições térmicas. Este estudo envolve múltiplas simulações para avaliar a estabilidade do método e extrair parâmetros relevantes, incluindo coeficientes de arrasto, sustentação e número de Nusselt, juntamente com campos de velocidade, pressão, vorticidade e temperatura. Através da comparação sistemática com a literatura existente, pretendemos validar os nossos resultados e contribuir para a melhoria contínua da precisão numérica neste domínio. Ao elucidar esses fenômenos complexos, nossa pesquisa visa fornecer informações valiosas para aplicações práticas em contextos industriais e de engenharia. O objetivo deste trabalho é analisar a combinação dos fenômenos de transferência de calor com rotação em cilindros isotérmicos e sua interação termofluido-estrutura. Para isso, foi desenvolvido um código C/C++ de baixo custo computacional (em termos de memória e recursos computacionais). Além disso, simulações numéricas indicaram que com o aumento do número de Reynolds, há um aumento no coeficiente de arrasto, destacando a influência significativa da distribuição de pressão a jusante do cilindro. Esta distribuição de pressão é fortemente afetada pela formação e desprendimento de vórtices, validando assim a metodologia.

Palavras-chave: Método da Fronteira Imersa, Cilindro Rotativo Isotérmico, Simulação Numérica, Escoamento Newtoniano Incompressível.

1. Introduction

A fluid can be conceptualized as a substance that undergoes continuous deformation when subjected to shear stress, regardless of its magnitude. Fluids play crucial roles across diverse domains, including natural phenomena and industrial processes, whether in isolation, as mixtures of different fluids, and/or in interaction with solid surfaces. Consequently, comprehending fluid dynamics within each application domain is of paramount importance.

Much of the research in fluid dynamics involves flows with intricate geometries, spanning applications in aerodynamics, bioengineering, hydraulic machines, porous media, and beyond. Prior to the advent of computers, the costs associated with experimental studies were largely confined to wind tunnels and field research. However, with the rise of computers and their high-capacity data processing and storage capabilities, aimed at tackling extensive calculations and numerical analyses, the costs linked to these investigations decreased, rendering numerical experiments more feasible and reliable. Yet, despite the undeniable strides in mathematical science, obtaining analytical solutions for nonlinear differential equations remains elusive, except in cases of highly simplified scenarios. Consequently, endeavors to analyze real-world fluid flow situations, beyond the realm of pure experimentation, continue to face the challenges posed by intricate technical requirements and the necessity for robust computational resources.

Mathematicians, physicists, engineers, and other researchers continually pioneer novel numerical simulation techniques, aiming to bridge the gap between numerical results and experimental findings. Computational Fluid Dynamics (CFD), in particular, leverages increasingly robust numerical methods and techniques to yield more precise results. However, tackling complex geometries remains a formidable challenge in CFD. Additionally, when boundaries are mobile, their motion disrupts flow dynamics, and conversely, flow dynamics affect boundary movement, compounding the complexity of the problem.

In methods relying on numerical meshes, the selection of an appropriate mesh is contingent upon the specific problem under investigation. Consequently, an algorithm designed, for instance, to handle curvilinear meshes may not be suitable for orthogonal meshes. Certain techniques utilize meshes that conform to the topology of the domain, such as adhering to a surface or a body of interest, known as adaptive meshes (referred to as Body-Fitted Mesh).

Numerous industrial challenges hinge on intricate geometries, posing complexities for computational modeling. Employing adaptive unstructured meshes to represent such intricate geometries can lead to intricate discretized formulations, escalating computational expenses and sometimes rendering numerical solutions impracticable. The mesh must intricately conform to both the object of study and the domain, with its generation often presenting nontrivial obstacles and potential errors between its constituent nodes. In the context of block discretization, inadequately constructed couplings between disparate domains may engender physical inconsistencies.

In addition to geometric complexity, another challenge arises in problems involving mobile and/or deformable bodies. Various proposals in the literature aim to address this class of problems, although none are universally definitive. Some methodologies rely on adaptive meshes to characterize such geometries, incorporating remeshing techniques for mobile and/or deformable bodies. Alternatively, other approaches are grounded in the concept of the Immersed Boundary Method. The latter offers certain advantages, such as the ability to simulate complex geometries within fixed orthogonal meshes, obviating the necessity for domain remeshing. In studies involving complex geometries immersed in flow, it is common to previously use a simpler geometry. This is usual for validating/improving methodologies or for a better understanding of flow dynamics.

There are still few studies regarding the flow around rotating circular cylinders with heating, with their examination initially addressed in the work of Badr and Dennis (1985). In this study, the authors investigated laminar flow with heat transfer by convection from a rotating circular cylinder immersed in a uniform flow. The analysis of phenomena resulting from the combination of rotation and heating, such as those found in flow meters, is rarely found in the literature due to the complexities involved in analyzing all parameters, including Reynolds, Strouhal, and Nusselt. Furthermore, works addressing flow around heated rotating cylinders are even scarcer compared to studies on flow around rotating cylinders without heating. Below are mentioned some relevant studies that investigate heat transfer, boundary layer, and natural and mixed convection in heated rotating cylinders.

Badr and Dennis (1985) considered the problem of heat-transfer by convection from an isothermal circular cylinder rotating around its own axis, immersed in a forced uniform flow. The authors reported that the temperature fields are strongly influenced by the cylinder rotation speed. They found that the total heat transfer coefficient tends to decrease as the cylinder speed increases. They attributed this to the presence of a layer of rotating fluid around the cylinder that separates the cylinder from the main stream flow.

Paramane and Sharma (2009) developed a numerical study focused on heat transfer by forced convection through a rotating circular cylinder with a constant rotation speed α , varying between 0 and 6. The flow transitions were shown for different Reynolds numbers and the different rotation rates. A block-structured mesh was used with a total number of 43.076 volumes. An elliptical mesh generation was used in the third block, where the cylinder is located. The authors verified and concluded that the decrease in the Nusselt number with the increase in rotational speed can be explained based on the fact that the fluid retained inside the vortex acts as a “buffer zone” for heat transfer between the cylinder and the free current and thus limits heat transfer.

Page *et al.* (2011) investigated the thermal behavior of a set of aligned cylinders subject to natural convection, with the objective of maximizing the heat transfer rate. A numerical method was used to solve the equations that describe the temperature and flow fields. The spacing between the aligned cylinders was optimized for each flow regime along with the cylinder rotation speed. The results also showed that there is an increase in the heat transfer rate of rotating cylinders compared to stationary cylinders. The results were compared with others available in the literature, showing convergence and precision.

Sharma and Dhiman (2012) developed research related to heat transfer by forced convection in a rotating circular cylinder for Prandtl number (Pr) values ranging from 0.7 to 100, in steady state. The methodology used was the second order Upwind Method, to approximate the convective terms of the equation of motion, while the diffusive term was discretized using the Centered Difference Method. Experimental results were presented for uniform heat conduction, for different values of the Prandtl number, for two fluids, water and ethylene glycol (automotive antifreeze). The commercial mesher GAMBIT was used and numerical calculations were performed using FLUENT for different conditions of Reynolds number, Prandtl number and rotation rates. The mesh near the surface of the cylinder was fine enough to resolve the boundary layer region. The isothermal patterns were presented, analyzed and compared with other results available in the literature, obtaining good numerical convergence.

Elghnam (2014) presented an experimental study of the dynamics of a flow over a rotating cylinder. Numerical calculations were performed using the FLUENT code based on the Finite Volume Method. The author aimed to analyze the flow dynamics by obtaining isothermal lines around the rotating cylinder, as well as the temperature distribution around the cylinder. The results of the heat transfer analysis were obtained as a function of dimensionless parameters, which are: Nusselt number (Nu), Reynolds number (Re) and Grashof number (Gr). Experimental measurements were performed in the range of 1.880 to 6.220 Reynolds numbers and 14.285 to 714.285 Grashof numbers, while numerical calculations were performed for Reynolds numbers ranging between 0 to 100.000 and Grashof numbers in the range of 100 to 1.000.000. A computational mesh generated by GAMBIT was used. For Reynolds numbers greater than 8.000, heat transfer rates were independent of the Grashof number (for $Gr \leq 100.000$). Both Grashof and Reynolds numbers influenced the rate of heat transfer. Furthermore, the effects of rotation on heat transfer were presented in terms of isothermal patterns, streamlines and Nusselt numbers. For the rotating circular cylinder, the maximum and minimum values shift in the direction of rotation. The difference between the maximum and minimum values of the Nusselt number decreased with increasing Reynolds number. For high Reynolds values, this difference tended to disappear and the Nusselt number became constant. As a result, it was found that the dependence of the Nusselt number on the Grashof number decreased as the value of the Reynolds number increased, and with the increase of this number for high values of Reynolds, this dependence disappeared.

Santos and Sales (2023) present an immersed boundary method for analyzing fluid-body interactions in two-dimensional (2D) flows around complex geometries, focusing on heat transfer and turbulence. The method uses a Eulerian mesh for the fluid and a Lagrangian mesh for the immersed body, ensuring non-slip conditions and accounting for heat exchange. The Navier-Stokes and energy equations are solved using Smagorinsky (LES) and Spalart-Allmaras (URANS) turbulence models. A computational code was implemented to calculate the lift, drag and Nusselt coefficients, with results compared to previous studies at different Reynolds numbers. This research advances the understanding of fluid-body interactions in complex geometries and thermofluid dynamics.

The following section describes the fundamentals of the Fronteira Imersa methodology, relevant to the physical-mathematical understanding of the method.

2. Theoretical Foundations

2.1 Introduction to the Immersed Boundary Methodology

Key physical phenomena in fluid mechanics find expression through mathematical modeling, typically comprising a set of nonlinear partial differential equations known as the conservation laws of fluid mechanics. These laws encompass the conservation of momentum, mass, and energy, collectively portraying the influences of forces on fluid dynamics and the associated energy exchanges across various flow regions. For Newtonian fluids, the viscous stress term can be correlated with the velocity field's deformation rates, enabling the description of flow dynamics through the Navier-Stokes equations. Advancements in high-performance computing and numerical techniques have facilitated the solution of numerous fluid mechanics problems.

In this work, the Immersed Boundary Method is used to model the presence of solid bodies immersed in a two-dimensional flow of an incompressible fluid. A force source term \vec{F} introduced in the Navier-Stokes equations is used to model the solid-fluid interface. Similarly, the heating of the immersed body is modeled by an energy source term Q . Thus, the methodology is based on a mixed formulation, with one mesh for the fluid (fixed Eulerian mesh) and another for the fluid-solid interface (Lagrangian mesh).

A particular code in C/C++ language was used to solve two-dimensional flows over mobile immersed bodies with heat transfer by forced convection. Flows around a stationary and rotating heated cylinder were simulated for different Reynolds numbers and different rotations. The computer program called *IBM-Code* is based on the explicit solution of the Navier-Stokes and Energy equations using the Euler method. Spatial discretizations were made using Centered Finite Differences. To correct pressure, the MSIP (Modified Strongly Implicit Procedure) method, proposed by Schneider and Zedan (1981), was used to solve linear systems. The vorticity, temperature, pressure and velocity fields and the drag and lift coefficients, the Nusselt number and the Strouhal number were obtained.

Next, the formulation that describes the Immersed Frontier Method used in the present work is presented.

2.2 Formulation for the fluid

The non-dimensionalized governing equations were written with the following assumptions:

- Laminar flow;
- Two-dimensional;
- Newtonian fluid;
- Incompressible flow, with constant properties. The buoyancy term, based on the Boussinesq approximation, does not appear, since in the present work only cases of forced convection are studied;
- Source terms in the energy and momentum equations based on the Immersed Frontier Method;
- Viscous dissipation and compression work are negligible in the energy equation.

In the present work, the calculation domain is modeled by a fixed Cartesian mesh that represents the fluid, as shown in Fig. 2.1. The equations of conservation of mass, motion and energy for incompressible flows of Newtonian fluids can be written in a dimensionless form, as follows:

$$\vec{\nabla} \cdot \vec{V} = 0, \quad (2.1)$$

$$\left[\frac{\partial \vec{V}}{\partial t} + (\vec{V} \cdot \vec{\nabla}) \vec{V} \right] = -\vec{\nabla} p + (Re)^{-1} \nabla^2 \vec{V} + \vec{F}, \quad (2.2)$$

$$\frac{\partial \theta}{\partial t} + \vec{V} \cdot \vec{\nabla} \theta = (Re Pr)^{-1} \nabla^2 \theta + Q, \quad (2.3)$$

where p is the pressure and \vec{V} is the velocity vector. The term \vec{F} is the Eulerian force field. This force source term \vec{F} models the existence of the interface immersed in the flow. Just as the source term \vec{F} “visualizes” the body in the flow, the Eulerian energy term Q is responsible for making the flow “feel” the presence of the heated solid interface, being non-zero in Eulerian meshes close to the Lagrangian mesh. The product between Re (Reynolds) and Pr (Prandtl) is known as the Péclet number and θ is the dimensionless temperature of the immersed interface.

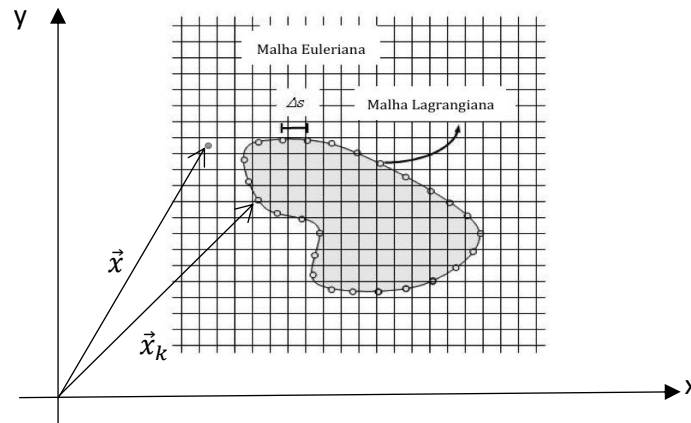


Fig 2.1- Illustrative representation of Eulerian (for the domain) and Lagrangian (for the interface) meshes for an immersed body with arbitrary geometry. ΔS is the distance between the Lagrangian points.

Both the force term \vec{F} and the energy term Q are obtained with the aid of the Dirac Delta function, being given by

$$\vec{F}(\vec{x}, t) = \int_{\Gamma} \vec{f}(\vec{x}_k, t) \delta(\vec{x} - \vec{x}_k) d\vec{x}_k, \quad (2.4)$$

$$Q(\vec{x}, t) = \int_{\Gamma} q(\vec{x}_k, t) \delta(\vec{x} - \vec{x}_k) d\vec{x}_k, \quad (2.5)$$

where $\vec{f}(\vec{x}_k, t)$ is the Lagrangian force density, calculated over the interface points, \vec{x} is the position of a Eulerian fluid particle and \vec{x}_k is the position of a Lagrangian point on the interface and q is the source of heating at the Lagrangian point \vec{x}_k at the immersed boundary. The Eqs. (2.4) and (2.5) model the interaction between the immersed boundary and the fluid, through the calculation of the force and energy field in the region where the immersed object is located. In the developed model, there are no constants to be adjusted, as in the models proposed by Peskin (1977) and Goldstein (1993), in addition, it is not necessary to use highly sophisticated algorithms to interpolate variables between two meshes or locate meshes neighboring this interface. This model allows representing the presence of the interface by solving the equations of motion and energy at each point of the Lagrangian mesh.

As the discretization of the Dirac Delta Function is not possible, it is replaced using a known distribution/interpolation function. This function aims to exchange information between the two meshes (Eulerian and Lagrangian), regarding pressure, speed, force and energy. The Eq. (2.6) shows the discrete formulation of the Eulerian force calculation, using this distribution/interpolation function

$$\vec{F}(\vec{x}) = \sum_k D_{ij}(\vec{x} - \vec{x}_k) \vec{f}(\vec{x}_k, t) \Delta s^2(\vec{x}_k), \quad (2.6)$$

where $\Delta s(\vec{x}_k)$ is the distance between two Lagrangian points, represented in Fig. 2.1. The D_{ij} is the distribution/interpolation function that in the present work has properties of a Gaussian function. Similarly, Q has the function of modeling the temperature field, being given by

$$Q(\vec{x}, t) = \sum_k D_{ij}(\vec{x} - \vec{x}_k) q(\vec{x}_k, t) \Delta s^2(\vec{x}_k). \quad (2.7)$$

The proposed formulation used by Peskin (1977) and McQueen (1994), with the distribution function D_{ij} represented by

$$D_{ij}(\vec{x}_k) = \frac{g_1 \left[\frac{x_k - x_i}{h} \right] g_1 \left[\frac{y_k - y_j}{h} \right]}{h^2},$$

where,

$$g_1(r) = \begin{cases} g_2(r), & \text{if } \|r\| < 1 \\ \frac{1}{2} - g_2(2 - \|r\|), & \text{if } 1 < \|r\| < 2 \\ 0, & \text{if } \|r\| > 2 \end{cases}$$

on what $g_2(r) = \frac{3-2\|r\| + \sqrt{1+4\|r\|-4\|r\|^2}}{8}$, and r represents $\left[\frac{x_k - x_i}{h} \right]$ or $\left[\frac{y_k - y_j}{h} \right]$. The term h is the size of the Eulerian mesh and (x_i, y_i) are the coordinates of a Eulerian point \vec{x} of the domain (Γ). This function is of the Gaussian type, for more details, Peskin and McQueen (1995). The force values \vec{F} and Q will be null throughout the calculation domain, with the exception of those close to the immersed interface, where they virtually model the presence of the heated immersed body, even though it has a complex geometry or is in motion.

In the next section, we present the formulation for the fluid-body interface, which plays an important role in the numerical simulation of fluid-body interactions in Computational Fluid Dynamics (CFD). This aspect involves defining how the fluid and body domains interact, ensuring adequate physical-mathematical representation of the boundary conditions, accounting for the phenomena of interest.

3. Formulation for the fluid-body interface

In the present work, an alternative model is used to calculate the density of the Eulerian force $\vec{F}(\vec{x}, t)$ and $Q(\vec{x}, t)$. The model used allows the calculation of $\vec{F}(\vec{x}, t)$ based on fluid-body interaction. This model is an alternative to models that use ad-hoc constants to evaluate the Lagrangian force. The model dynamically evaluates the force that the fluid exerts on the solid surface immersed in the flow and the thermal exchange between them.

The Lagrangian force $\vec{f}(\vec{x}, t)$ and the thermal source $q(\vec{x}, t)$ were evaluated separately, that is, for the Lagrangian force, a momentum balance was carried out on a fluid particle located near the fluid-body interface, while for the thermal source, the dimensionless energy equation was applied, which shows the iteration between the particle-fluid and the interface, as shown in Fig. 3.1, taking into account all terms of the Navier-Stokes equation. In this way, the density of the Lagrangian force can be expressed by Eq. (3.1).

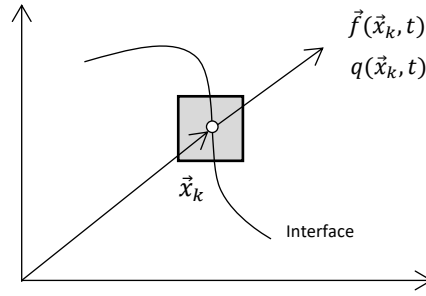


Figure 3.1 – Control volume located over a Lagrangian fluid particle.

The principle of conservation of momentum and energy is applied to any fluid particle that makes up a flow. These conservation principles must also be applied to fluid particles that are in contact with the fluid-body interface. Therefore, taking the particle illustrated in Fig. 3.1, through which an immersed interface is passing, we arrive at the following formulations:

$$\vec{f}(\vec{x}_k, t) = \underbrace{\frac{\partial \vec{V}(\vec{x}_k, t)}{\partial t}}_{\vec{f}_a} + \underbrace{\vec{\nabla} \cdot (\vec{V}(\vec{x}_k, t) \vec{V}(\vec{x}_k, t))}_{\vec{f}_i} - \underbrace{\frac{1}{Re} \nabla^2 \vec{V}(\vec{x}_k, t)}_{\vec{f}_v} + \underbrace{\vec{\nabla} p(\vec{x}_k, t)}_{\vec{f}_p}, \quad (2.8)$$

$$q(\vec{x}_k, t) = \frac{\partial \theta}{\partial t}(\vec{x}_k, t) + \vec{\nabla} \cdot (\vec{V}(\vec{x}_k, t) \theta(\vec{x}_k, t)) - \frac{1}{Re Pr} \nabla^2 \theta(\vec{x}_k, t), \quad (2.9)$$

the terms on the right side of Eq. (3.1) are respectively called *acceleration force* $\vec{f}_a(\vec{x}_k, t)$, *inertial force* $\vec{f}_i(\vec{x}_k, t)$, *viscous force* $\vec{f}_v(\vec{x}_k, t)$, and *pressure force* $\vec{f}_p(\vec{x}_k, t)$, Eq. (3.1) can be rewritten in simplified form in Eq. (3.2) below, given by

$$\vec{f}(\vec{x}_k, t) = \vec{f}_a(\vec{x}_k, t) + \vec{f}_i(\vec{x}_k, t) + \vec{f}_v(\vec{x}_k, t) + \vec{f}_p(\vec{x}_k, t), \quad (2.10)$$

it is important to note that these terms are calculated at the interface points, through interpolations of the pressure, velocity and temperature fields calculated in the Eulerian mesh.

3.1 The Indicator Function

An indicator variable $I(\vec{x}, t)$ is calculated with the purpose of identifying the position of the immersed body. It can also be used when it is necessary to exclude the region internal to the body, in the variable interpolation process. The indicator function used in the present work was proposed by Unverdi and Tryggvason (1992). It is an interface monitoring method, where the function is calculated over the entire domain or part of it, with the assignment of a unit value for points internal to the interface, and zero for external points and values between 0 and 1 for points of transition, i.e., points on the interface.

This function is based on a function $\vec{G}(\vec{x}, t)$ and can be expressed by

$$\vec{\nabla} I(\vec{x}, t) = \vec{G}(\vec{x}, t), \quad (3.1)$$

and the second member of the equality of Eq. (3.1) is given by

$$\vec{G}(\vec{x}, t) = \sum_k D_{ij}(\vec{x} - \vec{x}_k) \vec{n}(\vec{x}_k) \Delta S(\vec{x}_k), \quad (3.2)$$

where $\vec{n}(\vec{x}_k)$ is the vector normal to the surface.

Now, applying the divergent operator in Eq. (3.1), the Laplacian of the indicator function is obtained, being represented by

$$\vec{\nabla}^2 I(\vec{x}, t) = \vec{\nabla} \vec{G}(\vec{x}, t), \quad (3.3)$$

in this way, after solving the Poisson equation, Eq. (3.6), the field of the indicator function is obtained $I(\vec{x}, t)$ across the entire domain of calculation. To solve the linear system resulting from the discretization of Eq. (3.6), the MSIP (Modified Strongly Implicit Procedure) method was used.

3.2 Calculation of velocities, pressure and temperature

The derivatives of velocity, pressure and temperature are calculated by interpolating the velocity, pressure and temperature fields from the Eulerian mesh to Lagrangian points, which are not necessarily coincident with the Eulerian nodes. These calculations must take into account that the velocity of the fluid over the interface must be equal to the velocity at the interface, to guarantee the non-slip/slip condition. The velocity and pressure derivatives are calculated using the velocity and pressure fields obtained in Eq. (3.3) and the temperature is obtained using Eq. (3.2). Among several interpolation possibilities, we chose to interpolate $\vec{V}(\vec{x}_k, t)$ and $p(\vec{x}_k, t)$ at points close to the interface, as illustrated in Fig. 3.2. The interpolation method is shown next.

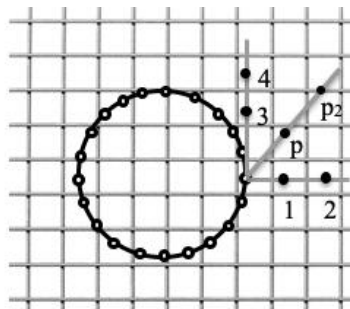


Figure 3.2 – Points used in the speed

For the interpolation process, the distribution/interpolation function D_{ij} was used to obtain the velocities, pressures and temperatures, already mentioned previously, by Eq. (2.8). In order to reduce computational cost, this function is evaluated only in a square region close to the point \vec{x}_k , therefore, for Eulerian points very far from the point \vec{x}_k analyzed, this function is null. The use of points internal to the interface, during the interpolation procedure, is physically coherent, since the internal flow is also solved by the Navier-Stokes equations. This in turn, being contrary to external flow, acts to recover the non-slip/slip condition. Figs. 3.3 (a) and (b), show an illustrative scheme of the interpolation procedure of the two velocity components, on auxiliary point \vec{x}_k .

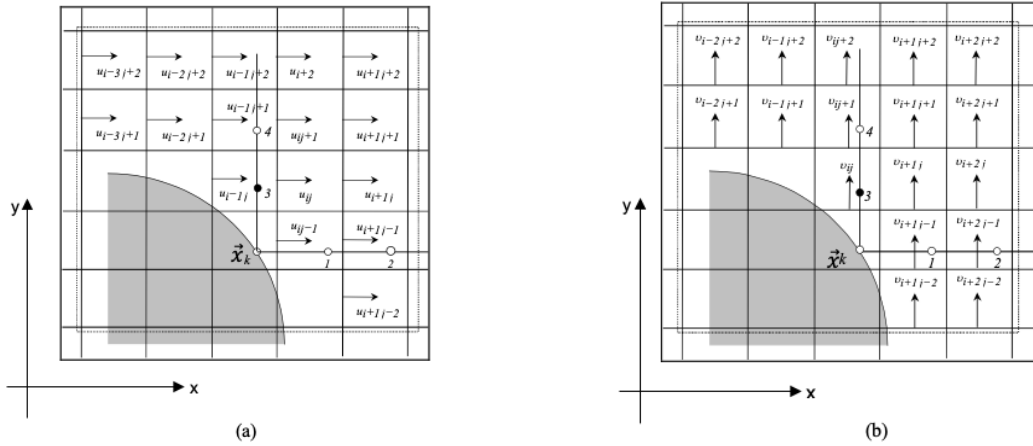


Figure 3.3 – Illustrative diagram of the velocity interpolation procedure at point 3: (a) for the u component and (b) for the v component.

Starting from each point \vec{x}_k of the interface, two straight lines are drawn parallel to the system of coordinate axes, towards the outside of the interface. In each direction, two distant points are marked Δx and $2\Delta x$ of the interface. This distance is necessary in order to prevent two auxiliary points from being allocated within the same Eulerian volume. Meshes that are at a distance greater than $2\Delta x$ of the Lagrangian point, do not contribute to the interpolation. For the calculation in time advance, a discretization is made expressed by $\frac{u_k - u_{fk}}{\Delta t}$ and $\frac{v_k - v_{fk}}{\Delta t}$, where u_k and v_k represent the interface velocities, u_{fk} and v_{fk} the velocities of the fluid over the interface, taking into account the velocities internal and external to the interface over the Eulerian mesh. Similarly, the temperature of the fluid at the interface is equal to the temperature of the solid, at each instant of time, being expressed by $\frac{\theta_k - \theta_{fk}}{\Delta t}$, where θ_k is the temperature at the interface and θ_{fk} the temperature of the fluid at the interface position.

The general equation for obtaining the velocity at Lagrangian points $\vec{V}(\vec{x}_k) = (u_{fk}, v_{fk})$ and at auxiliary points, it can be expressed by

$$\vec{V}(\vec{x}_k) = \sum_i D_{ij}(\vec{x}_i - \vec{x}_k) \vec{V}(\vec{x}_i), \tag{3.4}$$

on what $\vec{V}(\vec{x}_k)$ are the Lagrangian velocities, calculated at the auxiliary points and at the point \vec{x}_k by interpolation of Eulerian velocities $\vec{V}(\vec{x}_i)$.

For flow simulations over rotating cylinders, the tangential velocity components of the Lagrangian points can be calculated, according to the imposed angular velocity. The simulations were carried out for different values of specific rotation and some Reynolds numbers, aiming to identify variations in the aerodynamic coefficients, Strouhal and Nusselt numbers. In this case, the rotation is carried out only with the projection of the tangential velocity, obtained through the imposed angular velocity, in the x and y components of the velocity, at each Lagrangian point, as shown in Fig. 3.4.

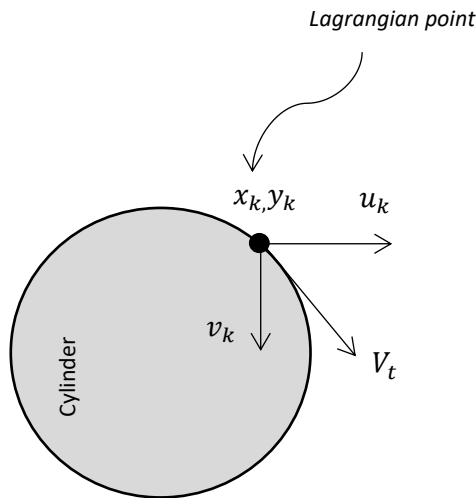


Figure 3.4 - Illustrative diagram of the projection of tangential velocity.

To calculate the derivatives of pressure and temperature at each Lagrangian point, it was necessary to obtain the value of pressure and temperature at the interface, at the point \vec{x}_k . To calculate pressure and temperature, an auxiliary point (P) was used, which is in a normal position at a distance Δx from the Lagrangian point. It can be seen in Fig. 3.5 that the pressure and temperature at this auxiliary point (P) belong to a Eulerian cell, both being transported to the interface. The process of obtaining pressure and temperature at the interface was also calculated using auxiliary points (1, 2, 3 and 4), calculating the respective derivatives in the x and y directions.

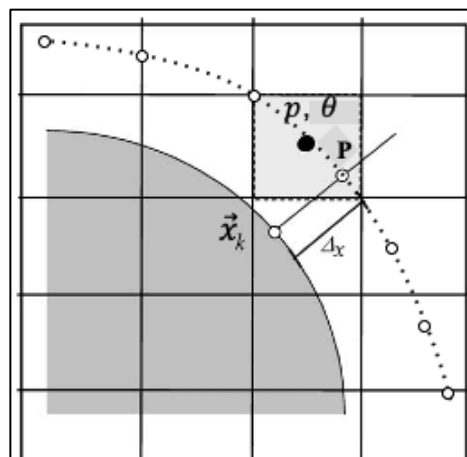


Figure 3.5 - Illustrative diagram of the interpolation procedure to obtain pressure and temperature.

The general equations for obtaining the pressure and temperature at points 1, 2, 3 and 4 are given by

$$p(\vec{x}_k) = \sum_{i,j} D_{i,j}(\vec{x}_i - \vec{x}_k) p(\vec{x}_i), \tag{3.5}$$

$$\theta(\vec{x}_k) = \sum_{i,j} D_{i,j}(\vec{x}_i - \vec{x}_k) \theta(\vec{x}_i), \tag{3.6}$$

where $p(\vec{x}_i)$ and $\theta(\vec{x}_i)$ are, respectively, the pressures and temperatures in the Eulerian mesh to be interpolated, $p(\vec{x}_k)$ and $\theta(\vec{x}_k)$ are the Lagrangian pressures and temperatures calculated at points 1,

2, 3 and 4. It was considered that the pressure gradient in the normal direction is zero and, therefore, the pressure at point \vec{x}_k is equal to the pressure at point **P**. This point was used to calculate the pressure and temperature on the surface and is schematized in Fig. 3.5.

The derivatives for calculating the pressure force are obtained using the Finite Difference Method, according to Eqs. (3.7) and (3.8):

$$\frac{\partial p}{\partial x} = \frac{p_2 - p_1}{x_2 - x_1}, \quad (3.7)$$

$$\frac{\partial p}{\partial y} = \frac{p_4 - p_3}{y_4 - y_3}. \quad (3.8)$$

Now, to calculate the temperature at each time step on the immersed boundary, $\theta(\vec{x}_k)$ was used and is interpolated according to Eq. (3.6). After interpolating the velocities, pressure and temperature at the interface and at the auxiliary points, the derivatives that make up the terms for calculating the Lagrangian source terms in the x and y directions are determined, with second-order Lagrange polynomials. Generically denoting the components of velocity or temperature by ϕ , the calculation of the first and second derivatives in the x and y directions, respectively, can be represented by

$$\frac{\partial \phi}{\partial x} = \frac{(x_i - x_k) + (x_i - x_2)}{(x_1 - x_2)(x_1 - x_k)} \phi_1 + \frac{(x_i - x_k) + (x_i - x_1)}{(x_2 - x_1)(x_2 - x_k)} \phi_2 + \frac{(x_i - x_1) + (x_i - x_2)}{(x_k - x_1)(x_k - x_2)} \phi_k, \quad (3.9)$$

$$\frac{\partial^2 \phi}{\partial x^2} = \frac{2\phi_1}{(x_1 - x_2)(x_1 - x_k)} + \frac{2\phi_2}{(x_2 - x_1)(x_2 - x_k)} + \frac{2\phi_k}{(x_k - x_1)(x_k - x_2)}. \quad (3.10)$$

And the derivatives in the y direction are given by

$$\frac{\partial \phi}{\partial y} = \frac{(y_i - y_k) + (y_i - y_4)}{(y_3 - y_4)(y_3 - y_k)} \phi_3 + \frac{(y_i - y_k) + (y_i - y_3)}{(y_4 - y_3)(y_4 - y_k)} \phi_4 + \frac{(y_i - y_3) + (y_i - y_4)}{(y_k - y_3)(y_k - y_4)} \phi_k, \quad (3.11)$$

$$\frac{\partial^2 \phi}{\partial y^2} = \frac{2\phi_3}{(y_3 - y_4)(y_3 - y_k)} + \frac{2\phi_4}{(y_4 - y_3)(y_4 - y_k)} + \frac{2\phi_k}{(y_k - y_3)(y_k - y_4)}, \quad (3.12)$$

where ϕ_1, ϕ_2, ϕ_3 and ϕ_4 are obtained through the interpolation of the closest Eulerian variables, as previously mentioned. The coordinates of the auxiliary points 1, 2, 3 and 4, and the coordinates of the point \vec{x}_k , are respectively the pairs, $(x_k, y_k), (x_1, y_1), (x_2, y_2), (x_3, y_3)$ and (x_4, y_4) . The points 1, 2, 3 and 4 are located outside the interface, so that the force calculation is independent of the flow properties inside it. The distance between points 1, 2, 3 and 4, as previously stated, is fixed at Δx . Therefore, the calculations of inertial, viscous force and pressure are independent of the flow inside the interface. The same is true for the energy equation.

The acceleration force, which is one of the terms of the total Lagrangian force, first installment of Eq. (2.8), was obtained through an approximation according to the expression

$$\vec{f}_a = \frac{\partial \vec{V}_k}{\partial t} = \frac{\vec{V}_k - \vec{V}_{fk}}{\Delta t}, \quad (3.13)$$

on what \vec{V}_k represents the interface velocity vector and \vec{V}_{fk} represents the fluid velocity vector at the same interface position. This acceleration force is called forcing acceleration and represents the portion with the greatest influence in the calculation of the total Lagrangian force, and can be interpreted as the portion that guarantees the non-slip/sliding condition. Similarly, the time derivative of temperature is given by $\frac{\partial \theta_k}{\partial t} = \frac{\theta_{fk} - \theta_k}{\Delta t}$.

An important calculation is that of the norm L_2 , which provides a difference between the fluid velocity at the interface \vec{V}_{fk} and the interface velocity itself \vec{V}_k . Strictly speaking, physically, the norm must be null, so that the non-slip/slip condition is satisfied, however, a small variation occurs due to the imposition being made explicitly, both for the non-slip/slip conduction. as for the temperature imposed at the interface. The value of the norm L_2 is given by Eq. (3.14), and a value around 10^{-3} is considered acceptable, according to Vedovoto (2007):

$$L_2 = \frac{\sqrt{\sum [(u_k - u_{fk})^2 - (v_k - v_{fk})^2]}}{n_{p\ell}}, \quad (3.14)$$

where $n_{p\ell}$ is the number of Lagrangian points on the immersed interface.

3.3 Dimensionless Parameters and Nondimensionalization of Equations

Some dimensionless parameters that characterize the forced flow over a heated rotating cylinder are presented below, such as the pressure coefficient, the Strouhal number and the drag and lift coefficients, the Reynolds number and the Nusselt number. The pressure coefficient is defined as $C_p = \frac{(p - p_\infty)}{0,5 \rho U_\infty^2}$, where p_∞ is the pressure of the free stream, far from the immersed interface. The dimensionless time scale is defined as $T = \frac{U_\infty t}{d}$. The drag force on a body submerged in a fluid arises from the pressure distribution and the shear stress distribution along the body. The drag coefficient is defined as $C_D = \frac{F_d}{\frac{1}{2} \rho U_\infty^2 d}$, where F_d is the drag force per unit length, calculated using the Lagrangian force component (N/m^3), in the direction of flow.

The drag force can be calculated using the x component of the Lagrangian force, in the flow direction, as $F_d = - \int_0^L f_x ds$, where f_x is the x component of the Lagrangian force, acting on the fluid and ds is the length element at which the point \vec{x}_k is centered, and L is the length of the interface. The negative sign is due to the fact that drag and lift are due to the forces exerted by the fluid on the immersed interface.

The lift force arises from the oscillation of the vortices formed downstream of the cylinder. Analogously to the drag coefficient, the lift coefficient is defined by $C_\ell = \frac{F_\ell}{0,5 \rho U_\infty^2 d}$, where F_ℓ is the support force, which is calculated by the y component of the Lagrangian force, transverse to the main flow direction, as $F_\ell = - \int_0^L f_y ds$, where f_y is the y component of the Lagrangian force.

Another important dimensionless parameter is the Strouhal number, which is defined as the dimensionless frequency of vortex shedding $St = \frac{f d}{U_\infty}$, where f is the dimensional frequency of formation and detachment of vortices. This frequency can be obtained by the Fast Fourier Transform (FFT) of the lift coefficient signal (not discussed in this work).

Another parameter is the Nusselt number, which, physically analyzed, is a quantity used to determine the heat transfer coefficient by convection through conduction, based on dimensional analysis, in which it is used to determine parameters through similarity relationships. Thus, it is common to express the Nusselt number in dimensionless form as $Nu = \frac{h.d}{k_f}$, where h is the heat-transfer coefficient, and d is an interface length, where for complex shapes it is defined as the volume of the body divided by its surface area, and k_f is the thermal conductivity of the fluid. The local Nusselt number was obtained by the temperature gradient in the direction normal to the interface by $Nu = \frac{\theta_{p2} - \theta_p}{\Delta n}$, where $\Delta n = \Delta x$.

The average of this number can be determined around the immersed surface, with the average of the Nusselt number calculated around the surface of the immersed cylinder using the following mathematical formulation

$$\overline{Nu} = \frac{1}{\pi d} \int_{\Gamma} Nu(\vec{x}_k, t) ds. \quad (3.15)$$

The non-dimensionalization of the equations is done with the aim of obtaining the parameters involved above. The Navier-Stokes equations for incompressible flows can be made from dimensionless quantities, according to Hughes *et al.* (1999):

$$u = \frac{u'}{U_{\infty}}, v = \frac{v'}{U_{\infty}}, p = \frac{p}{\rho U_0^2}, x = \frac{x'}{d}, y = \frac{y'}{d}, \theta = \frac{T - T_{\infty}}{T_c - T_{\infty}}.$$

where, u', v' are the dimensional velocities; u, v are the dimensionless velocities; U_{∞} is the uniform velocity at the domain entry, and T_{∞} is the fluid temperature away from the cylinder.

3.4 Geometric parameters for an immersed circular cylinder

The entire process of modeling the immersed interface involves determining the coordinates of the points that make up the interface and some geometric parameters such as the normal and the distance between points. Next, this process is detailed for an immersed circular cylinder. First, the central position of the interface is defined, that is, the coordinates C_x and C_y from the center of the cylinder. For a circular interface, the initial coordinates of the Lagrangian points are determined through the angle between consecutive points, which is kept constant. For a given number of Lagrangian points ($np_{\ell k}$), there is the angle $\Delta\theta$, Fig. 3.6, calculated as follows

$$\Delta\theta = \frac{2\pi}{np_{\ell k}}, \quad (3.16)$$

and

$$\theta_{K+1} = \theta_K + \Delta\theta. \quad (3.17)$$

The initial coordinates of the points are

$$x_k = C_x + R \cos(\theta_k), \quad (3.18)$$

$$y_k = C_y + R \sin(\theta_k), \quad (3.19)$$

where, R is the radius of the cylinder, x_k and y_k are the coordinates, x and y from the point k ; C_x and C_y are the coordinates x and y from the center of the circular interface. In order to calculate the Lagrangian force field it is necessary to know the geometric parameters of the circular interface. The normal vector is calculated over each point, which has components in the x and y direction of the Cartesian mesh, and the arc length, centered over each point, as illustrated in Fig. 3.6 (a) and (b).

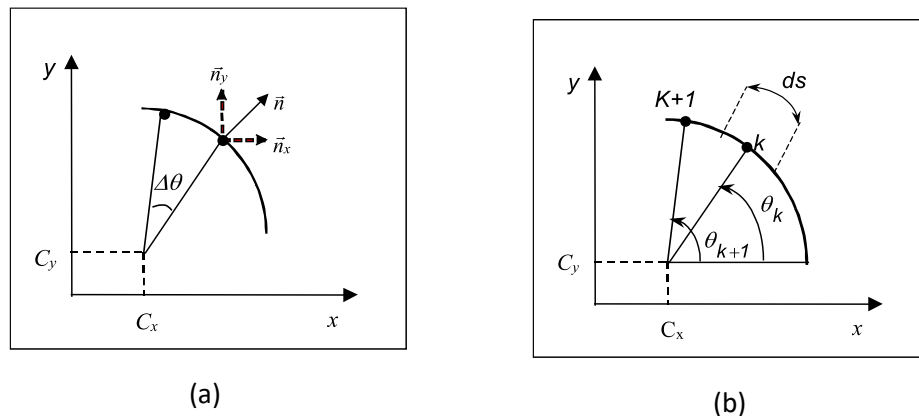


Figure 3.6 – Schematic representation of normal vectors over a Lagrangian point (a) and representation of the arc length and angles of two consecutive points (b).

The interface can be modeled through a parametric vector equation of the type

$$\vec{R}(p) = g(p)\vec{i} + h(p)\vec{j}. \quad (3.20)$$

To calculate the components $g(p)$ and $h(p)$, Lagrange interpolating polynomials of degree n are used over a set of $n + 1$ points. Therefore, we have:

$$g_n(p) = \sum_{k=0}^n L_k(p)x_k(p_k), \quad (3.21)$$

$$h_n(p) = \sum_{k=0}^n L_k(p)y_k(p_k), \quad (3.22)$$

where,

$$L_K(p) = \prod_{\substack{j=0 \\ j \neq k}}^n \frac{p - p_j}{p_k - p_j}, \quad (3.23)$$

the points $x_k(p_k)$ and $y_k(p_k)$ are the coordinates of the interface points, which can be defined by $\{x_k(p_k), y_k(p_k)\}$, with $k = 0, \dots, n$ and $p_k = k$. One can, therefore, calculate the normal and arc length by the following expressions, respectively:

$$\vec{n}(\vec{x}_k) = \frac{-h' \vec{i} + g' \vec{j}}{\sqrt{(h')^2 + (g')^2}}, \quad (3.24)$$

$$ds(\vec{x}_k) = \frac{1}{4} \left(\sqrt{g'^2(\vec{x}_{k-1}) + h'^2(\vec{x}_{k-1})} + 2\sqrt{g'^2(\vec{x}_k) + h'^2(\vec{x}_k)} + \sqrt{g'^2(\vec{x}_{k+1}) + h'^2(\vec{x}_{k+1})} \right), \quad (3.25)$$

where (') is the derivative with respect to the parameter p . A Eulerian mesh stability criterion was used, so that $0,9 \leq \frac{\Delta s}{\Delta x} \leq 1,1$; where Δs is the distance between two consecutive Lagrangian points, and Δx the size of the Eulerian mesh. This range of values allows for greater numerical stability. In this work, a 4th degree Lagrange polynomial was used and therefore, a series of 5 points to calculate the geometric parameters. An example can be given of calculating the components $g(p)$ and $h(p)$ for point 2, as illustrated in Fig. 3.7, using five points $(p_0, p_1, p_2, p_3, p_4)$ this way

$$g'_4(p_2) = \frac{[x_0(p_0) - 8x_1(x_1) + 8x_3(p_3) - x_4(p_4)]}{12}, \quad (3.26)$$

$$h'_4(p_2) = \frac{[y_0(p_0) - 8y_1(x_1) + 8y_3(p_3) - y_4(p_4)]}{12}, \quad (3.27)$$

being $x_0(p_0), y_0(p_0), x_1(p_1), y_1(p_1), x_3(p_3), y_3(p_3), x_4(p_4)$ and $y_4(p_4)$ the coordinates of the Lagrangian points, p_0, p_1, p_3, p_4 , respectively.

The Eqs. (3.26) and (3.27) are substituted into Equations (3.24) and (3.25) to determine the geometric parameters of the Lagrangian point of point 2, Fig. 3.7. The same procedure is done for all points (x_k, y_k) , so that the components of the normal can be obtained. In the present work, the rotational movement of the cylinder does not change the distance $\Delta s(\vec{x}_k)$ between the Lagrangian

points, as they all move with the same angular velocity. In simulations where the interface deforms, values must be recalculated at each instant.

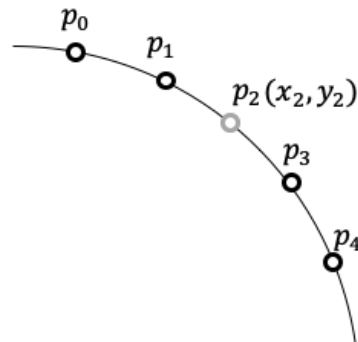


Figure 3.7 – Illustration of the five points used to calculate the normal \vec{n} and arc length Δs at point 2.

4. Numerical method

When conducting mathematical modeling pertaining to physical engineering problems, differential equations emerge as a crucial tool for decoding and understanding these phenomena. Typically, exact solutions for flows are confined to simplified scenarios due to the prevalence of nonlinear equations in mathematical models. Consequently, numerical methods serve as invaluable complements to experiments, bridging the gap between numerical and experimental results.

The numerical analysis of a flow hinges upon determining variable fields of interest at discrete points. Discretization methods aim to substitute differential equations with a set of algebraic equations, yielding the values of interest at discrete points across the flow domain. This process yields a system of equations to be solved at each domain point where the problem's solution is sought. Upon solving this system, an approximate solution to the problem emerges. As the number of mesh points increases, the solution to the discretized equations converges towards the exact solution of the differential equation.

The IBM-Code, developed in C/C++, comprises subroutines dedicated to solving individual steps of the solution method independently. The main program, responsible for variable declaration, orchestrates all subroutine calls. Through a data file, users can specify initial boundary conditions and select the interface type (such as a circular cylinder) immersed in the flow. Eulerian variables are represented as matrices matching the dimensions of the Eulerian mesh, while Lagrangian variables are represented as vectors. The program's architecture facilitates data file saving at any point, enabling the resumption of interrupted calculations due to power outages.

Conservation equations are discretized using Finite Differences, involving the approximation of partial differential equation derivatives via Taylor Series truncation. Solving the nonlinear equations of momentum conservation for incompressible flows entails coupling pressure and velocity fields. Among various methods, the Fractional Step Method, initially proposed by Chorin (1968) and further refined by Kim and Moin (1985), demonstrates promising results in terms of numerical convergence and mass conservation. Only one iteration per time step is required for the velocity fields to satisfy continuity.

In this study, the Centered Finite Difference Method was employed for discretization on a non-uniform mesh, while the first-order Euler Method was utilized for temporal discretization. The Navier-Stokes and energy equations were solved explicitly. The discretized pressure correction expression yields a linear system, tackled using the MSIP Method (Modified Strongly Implicit Procedure), pioneered by Schneider and Zedan (1981).

Below, the research provides a concise overview of the fractional step method and the temporal discretization employed, drawing parallels with the equation of motion.

4.1 The Fractional Step Method

The Fractional Step Method represents a numerical procedure for coupling pressure and velocity fields. Its role is to numerically solve the Navier-Stokes and continuity equations, coupling them to provide final velocity and pressure fields. Like many numerical solution methods for the Navier-Stokes equations, the basic principle involves a two-step process: a predictor and a corrector.

The predictor step is straightforward, utilizing discretized derivatives. An uncorrected velocity field is obtained from fields taken at previous time steps. The corrector step, on the other hand, ensures mass conservation by solving a Poisson equation for pressure correction terms.

After these two steps are applied, new (real) velocity and pressure fields are obtained. This procedure progresses in time, meaning that the final fields for a given time step act as initial fields for the next time step. With the estimated velocity fields and pressure correction, a linear system is formed and solved using the MSIP method.

The Eq. (2.2), in indexical form, for the velocity in the current iteration is rewritten as:

$$\left[\frac{u_i^{n+1} - u_i^n}{\Delta t} + \frac{\partial(u_i u_j)^n}{\partial x_j} \right] = -\frac{\partial p^{n+1}}{\partial x_i} + \frac{\partial}{\partial x_j} + \frac{1}{Re} \left(\frac{\partial u_i^n}{\partial x_j} + \frac{\partial u_j^n}{\partial x_i} \right) + F_i^n, \quad (3.28)$$

where $n + 1$ represents the current iteration. Approximations of the velocity components (\bar{u}_i) which are carried out using the pressure, velocity and force fields, calculated in the previous iteration, are given by

$$\left[\frac{\bar{u}_i^{n+1} - u_i^n}{\Delta t} + \frac{\partial(u_i u_j)^n}{\partial x_j} \right] = -\frac{\partial p^n}{\partial x_i} + \frac{\partial}{\partial x_j} + \frac{1}{Re} \left(\frac{\partial u_i^n}{\partial x_j} + \frac{\partial u_j^n}{\partial x_i} \right) + F_i^n, \quad (3.29)$$

the notation \bar{u}_i indicates approximate/estimated velocity

Now, subtracting Eq. (3.28) from Eq. (3.29), we obtain:

$$\frac{\bar{u}_i^{n+1} - u_i^{n+1}}{\Delta t} = -\frac{1}{\rho} \frac{\partial(p^{n+1} - p^n)}{\partial x_i}. \quad (3.30)$$

Then, applying the divergent $\frac{\partial}{\partial x_i}$ on both sides of Eq. (3.30), we have:

$$\frac{\partial}{\partial x_i} \left[\frac{\bar{u}_i^{n+1} - u_i^{n+1}}{\Delta t} \right] = \frac{\partial}{\partial x_i} \left[-\frac{1}{\rho} \frac{\partial(p^{n+1} - p^n)}{\partial x_i} \right], \quad (3.31)$$

or yet,

$$\frac{1}{\Delta t} \left[\frac{\partial \bar{u}_i^{n+1}}{\partial x_i} - \frac{\partial u_i^{n+1}}{\partial x_i} \right] = \frac{1}{\rho} \frac{\partial}{\partial x_i} \left(\frac{\partial p'^{n+1}}{\partial x_i} \right), \quad (3.32)$$

where $\partial p'^{n+1}$ is the pressure correction, written as:

$$p'^{n+1} = p^{n+1} - p^n. \quad (3.33)$$

Calculating the divergence is important because it expresses the conservation of mass. For the flow of an incompressible fluid, the value of the divergence is used (in numerical methods) as a

guarantee of the conservation of mass throughout the computational domain. The velocity field must satisfy the continuity equation. With this condition defined, the second term on the left side of Eq. (3.32), namely, $\left(\frac{\partial \bar{u}_i^{n+1}}{\partial x_i}\right)$ will be cancelled. Therefore, Eq. (3.32) can be rewritten as follows:

$$\frac{1}{\Delta t} \frac{\partial \bar{u}_i^{n+1}}{\partial x_i} = \frac{1}{\rho} \frac{\partial^2 p'^{n+1}}{\partial x_j \partial x_j}. \quad (3.34)$$

Rearranging the terms of Eq. (3.34), Poisson's equation for pressure correction (p') is obtained whose source term is the divergence of the approximate/estimated speed, and can be written in the following forms:

$$\frac{\partial^2 p'^{n+1}}{\partial x_j \partial x_j} = \frac{\rho}{\Delta t} \frac{\partial \bar{u}_i^{n+1}}{\partial x_i}, \quad (3.35)$$

or

$$\nabla^2 p'^{n+1} = \frac{\rho}{\Delta t} (\vec{\nabla} \cdot \bar{\mathbf{u}}^{n+1}). \quad (3.36)$$

Therefore, the approximate/estimated velocity field is obtained through Eq. (3.28) and the pressure correction field, through the resolution of the linear system, generated by the discretization of Eq. (3.35) or Eq. (3.36). From Equation (3.30), the corrected speed for the current iteration is calculated, given by

$$u_i^{n+1} = \bar{u}_i^{n+1} - \frac{\Delta t}{\rho} \frac{\partial p'^{n+1}}{\partial x_i}. \quad (3.37)$$

It is important to comment that a predominant advantage of using the *Fractional Step Method* arises from the method's own deduction, it is the guarantee of low Continuity residues $\left(\frac{\partial u_i^{n+1}}{\partial x_i} \cong 0\right)$ right after the system solution. This allows for faster temporal advancement, that is, a quick and direct passage to the next instant of time. Regarding explicit temporal advances, care was taken in assigning values for time increments. Large increments are strong conditions for instability in the code. In this context, the calculations were initialized with steps of 10^{-6} s, which were gently elevated to values of 10^{-4} s. Regarding the equations presented in the previous item, they were discretized using the Centered Differences method in space, more details, can be seen at Santos (2014).

5. Results

Using the Immersed Frontier Method implemented in the IBM-Code, it was possible to carry out simulations of two-dimensional flows around a heated body immersed in the flow. Simulations of flows around a heated cylinder with constant temperature and rotation. They were performed for Reynolds numbers ranging from 80 to 200. The cylinder was maintained at a constant dimensionless temperature equal to 1 ($\theta = 1$), while the fluid has an initial temperature $\theta = 0$. The specific rotation value (α) was varied from 0 to 4.0 in order to analyze its influence on heat transfer and force coefficients. Then the results were compared with the literature, including the experiments carried out by Carvalho (2003). The vorticity, temperature and pressure fields, the lift and drag coefficients, the Strouhal number and the Nusselt number are presented for different Reynolds numbers and specific rotations.

The present work was restricted to simulating flows around a heated cylinder of diameter d immersed in an incompressible fluid with constant properties. The simulations were carried out with the rotary movement of the cylinder, and with this, it was possible to numerically validate the methodology and carry out an analysis of the influence of rotation on the thermal field.

For all simulations, a rectangular domain of dimensions $55d \times 30d$ was used, (Fig. 5.1), since a previous analysis of its dimensions and also the refinement of the mesh was already carried out in the work of Lima and Silva (2003). These dimensions were determined numerically to minimize the influences of the domain on the flow around the cylinder and at the same time, minimize the unnecessary number of nodes. The central coordinates of the cylinder are $16.5d \times 15d$ in x and y .

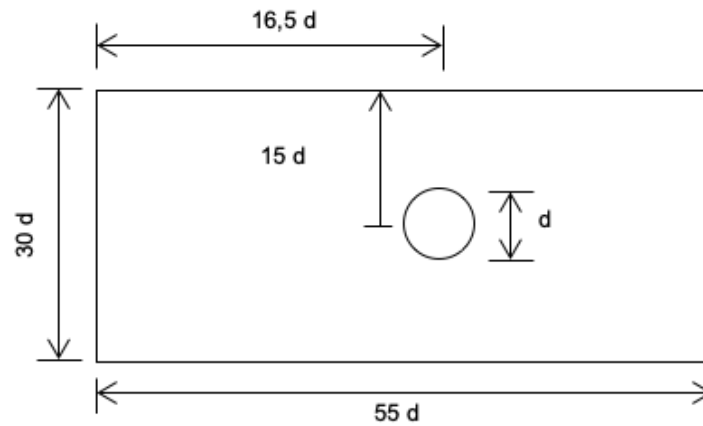


Figure 5.1 – Diagram illustrating the dimensions of the calculation domain.

A non-uniform mesh of 318×164 points was used in order to better capture the effects of rotation along with a total of 201 points for the Lagrangian mesh. The mesh is uniform in the cylinder region, maintaining a minimum of 30 meshes inside. The time step used in the calculation process is in the range from $1,0 \times 10^{-6}$ s (minimum) to $1,0 \times 10^{-4}$ s (maximum), is calculated dynamically with the Friedrichs – Lewy stability criterion, better known as the CFL criterion, necessary for time-explicit solutions. Then, numerical simulations were carried out for the respective Reynolds numbers varying the $80 \leq Re \leq 200$, for different values of α . Flow analyzes were carried out for different angular velocities, imposed clockwise and counterclockwise, for the respective Reynolds numbers already mentioned above. The temperature difference between the cylinder and the fluid was kept constant. The flow develops from left to right, with a uniform velocity profile imposed at the domain entrance and a damping function at the domain exit to prevent the return of vortices at the exit. The Prandtl number was kept constant at 0.7 (air) for all simulations.

For the lateral boundaries of the domain, free boundary conditions were used, that is, zero derivative of the velocities. At the entrance to the domain, a uniform velocity profile was imposed (U_∞) and at the exit, zero derivative for the velocities. The boundary conditions are given by (a) Input: $u = U_\infty$ and $v = 0$; (b) Output: $\frac{\partial u}{\partial x} = \frac{\partial v}{\partial x} = 0$; (c) Lower and upper border: $\frac{\partial u}{\partial y} = \frac{\partial v}{\partial y} = 0$. For pressure, the boundary conditions used were of the Neumann type at the entrance and Dirichlet at the exit and on the sides of the domain, as shown in the following expression: (a) domain entry: $\frac{\partial P}{\partial x} = 0$; and (b) output and lower and upper borders: $p = 0$. For temperature, the conditions are analogous to velocity, that is: (a) domain entry: $\theta = 0$; and output and sides: $\frac{\partial \theta}{\partial x} = 0$; $\frac{\partial \theta}{\partial y} = 0$.

All simulations were carried out until the regime was established, that is, in all simulations a time of approximately 48h was spent for the established flow regime to be reached, which was verified through the graphs of the force coefficients in function of time. The computer used has an Intel(R) Core (TM) i5-2400 CPU 3.10 GHz processor with 4.00 GB with a 64-bit operating system. The simulations with different rotations were started with a stationary cylinder and after approximately $t = 0.05$ s the rotation started. This procedure was adopted to ensure the calculated force field was already capable of reproducing the immersed cylinder before rotation began. Some

results show the distribution of the variable over the surface of the cylinder. By convection, the angle θ was adopted, which defines the positions of the points on the body and varies counterclockwise, starting from the upstream stagnation point, as shown in Fig. 5.2.

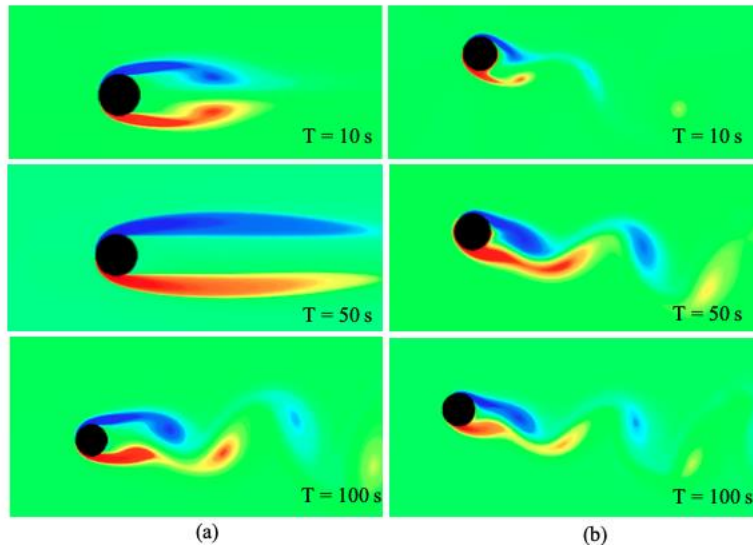


Figure 5.2 – Illustrative diagram for varying the angle θ on the cylinder.

5.1 Visualization of flow fields

Next, in Figs. 5.3 and 5.4, at different moments of time, the vorticity fields (which provide a considerable notion about the movement of fluids) are presented, for Reynolds (Re) numbers equal to 100 and 200, respectively, around a stationary and rotating (non-isothermal) cylinder. The right column (column (a)) represents the different time instants for the simulation with specific rotation $\alpha = -1,5$ (counter-clockwise).

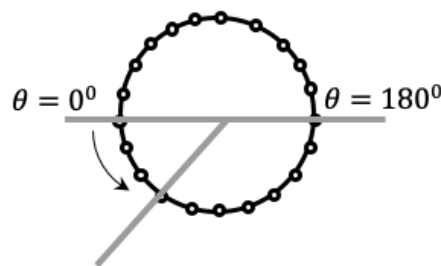


Figure 5.3 – Vorticity fields for $Re = 100$. The left column (a) represents the stationary cylinder with $\alpha = 0$. The right column (b) represents the rotating cylinder for $\alpha = -1,5$.

In flow with a stationary cylinder, the initial moments are marked by the appearance of a recirculation bubble behind the cylinder. This region where the fluid is "trapped" increases constantly ($T = 50$) until a maximum length. Then the process of detachment of the first vortices begins.

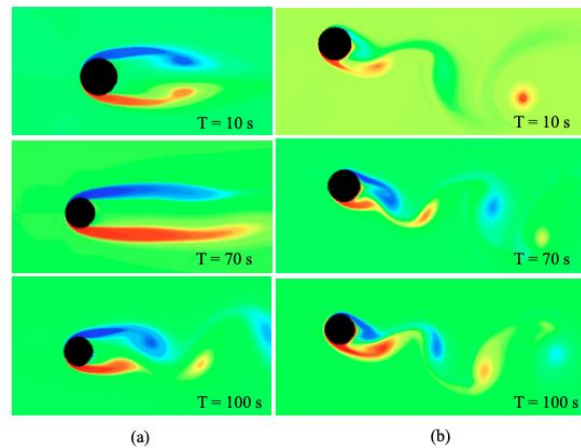


Figure 5.4 – Vorticity fields for $Re = 200$. The left column (a) represents the stationary cylinder with $\alpha = 0$.
The right column (b) represents the rotating cylinder for $\alpha = -1.5$.

It is known that the process of generation and shedding of vortices occurs due to the instabilities of the shear layers, which in turn depend on the geometry of the body and the Reynolds number. Due to the approximation that occurs in the opposing shear layers, this causes vortices to be generated and transported downstream, causing the process to repeat itself periodically in an alternating manner, in the case of the stationary cylinder. It can be seen in Figs. 5.3 and 5.4 that the stationary cylinder has an elongated wake, with vortex shedding starting after approximately $T = 80$.

The rotation anticipates the detachment, destabilizing the flow, causing the Von Kármán wake to appear in the initial moments. For these values of Reynolds 100 and 200 and $\alpha = -1.5$, vortex shedding is not inhibited and the wake tilts downwards, in the direction of rotation. Visually, it is observed that with an increase in the Reynolds number, this causes the vortices to detach closer to the cylinder, reducing drag due to the fact that the vortices hit with more intensity behind the cylinder.

5.2 Qualitative Comparison

In Figure 5.5 they are compared with the experimental results obtained by Carvalho (2003) for $Re = 115$ and different values of α , with the results obtained in this work. The cylinder rotates clockwise. The results of the numerical simulations for the same Reynolds number, and the same rotations, are presented in the right column of Fig. 5.5.

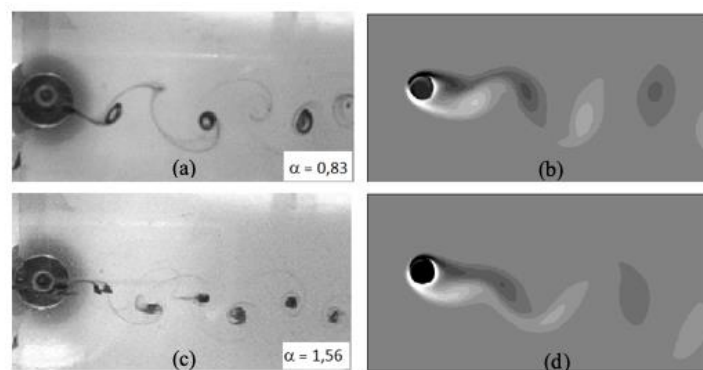


Figure 5.5 – Qualitative comparison between the experimental result of Carvalho (2003). In the right column, the numerical results of the present work; in the left column (laboratory experiment) for $Re = 115$ with different specific rotations.

A good similarity can be noted between the numerical results of the present work and the experimental results of Carvalho (2003). The wake formed downstream has a similar inclination in both studies, in addition, for values of $\alpha \leq 1.56$, the consecutive vortices close to the cylinder also have similar distances. The critical α value for $Re = 115$ was $\alpha = 2.02$, while the experimental one was between 2.02 and 2.27. For more details, see Santos (2014).

In Fig. 5.6, the instantaneous temperature isolines (left column) and the current lines (right column) for $Re = 200$ are presented. In the figure below, the time instant ($T=120$) and the value of α are fixed.

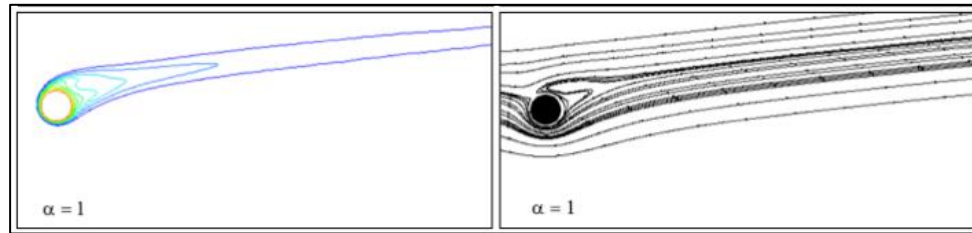


Figure 5.6 – Temperature isolines (left column) and streamlines (right column) for $Re = 200$, with $\alpha = 1$.

This figure illustrates the effect of rotation on the thermal field and velocity field. The streamline fields prove that the increase in α tends to increase the region close to the cylinder where the fluid is trapped. The volume of this insulation fluid directly interferes with the heat transfer close to the cylinder and consequently with the Nusselt number distributions. Rotation changes the shape of the temperature isolines and also their orientation, as the belt tends to rotate in the same direction as the cylinder rotation. One can also observe a change in the position of the stagnation point at ($\theta = 0^\circ$). The increase in α causes this point to move in the opposite direction to the rotation, which is seen in the graphs of the local distributions of the Nusselt number and the pressure coefficient.

Next, the results of the aerodynamic and pressure coefficients are presented, as well as the Strouhal and Nusselt numbers. Firstly, graphs of the evolution over time of the coefficients presented in different ways are shown. Then, the local distributions on the cylinder surface and the average values obtained are shown.

5.3 Results of drag, lift coefficients and Nusselt numbers

Table 5.1 below presents some of the results obtained in the present work for the average values (time averages) of the drag coefficients, for Reynolds numbers equal to 80, 100 and 200 simulated numerically, compared with the numerical data from Ren *et al.* (2013), Liu and Ding (2015), Lima and Silva (2003) and Ye *et al.* (1999), for the stationary case, that is, for $\alpha = 0$.

Authors	Present Work	Ren <i>et al.</i> (2013)	Liu and Ding (2015)	Lima and Silva (2003)	Ye <i>et al.</i> (1999)
Re					
80	1.395	-	-	1.40	1.37
100	1.368	1.346	1.350	1.390	-
200	1.348	-	-	1.390	-

Table 5.1 – Comparison between the average values of the drag coefficients for $Re = 80$, $Re = 100$ and $Re = 200$.

Table 5.2 shows the results obtained in the present work for the average Nusselt in comparison with some results obtained by Baranyi (2003) and Mahir *et al.* (2008), Paramane and Sharma (2009) and Shrivastava *et al.* (2012). Several correlations can be obtained for the average Nusselt number, in Incropera *et al.* (6th edition, pg. 267, 2008) the empirical correlation adopted in the present work was that of Hilpert, which considers global average conditions, being represented by

$$\bar{Nu} = c Re_D^m Pr^{\frac{1}{3}}$$

where, $Re_D : 40 - 40.000$, $c = 0,683$ and $m = 0,466$.

Re	Autores	
80	Presente Trabalho	4,6733
	Paramane e Sharma (2009)	4,5000
100	Presente Trabalho	5,1855
	Baranyi (2003)	5,1320
	Mahir et al., (2008)	5,1790
200	Presente Trabalho	7,1625
	Mahir et al., (2008)	7,4740
	Shrivastava et al. (2012)	7,1600

Table 5.2 – Comparison between results for the average Reynolds number and Strouhal number, for $\alpha = 0$.

A good agreement is observed in the values obtained, with differences of around 3%, which confirms the validity of the method for the stationary and non-stationary cases. In this way, these calculations with immersed geometries were validated with regard to the choice of mesh refinement and domain dimensions, so as not to influence the obtained values of the aerodynamic coefficients.

Next, the results of the temporal evolution of the coefficients and the Nusselt number are presented.

5.4 Temporal evolution of coefficients and dimensionless numbers

The Figure 5.7 shows the evolution of the drag coefficient as a function of dimensionless time (T), for Reynolds numbers equal to $Re = 80$ and 200 , for different values of α . For the simulations with the stationary cylinder ($\alpha = 0$), the time taken to reach an established flow regime was longer. The increase in rotation caused the shedding of vortices to be brought forward and consequently the periodic regime was reached earlier.

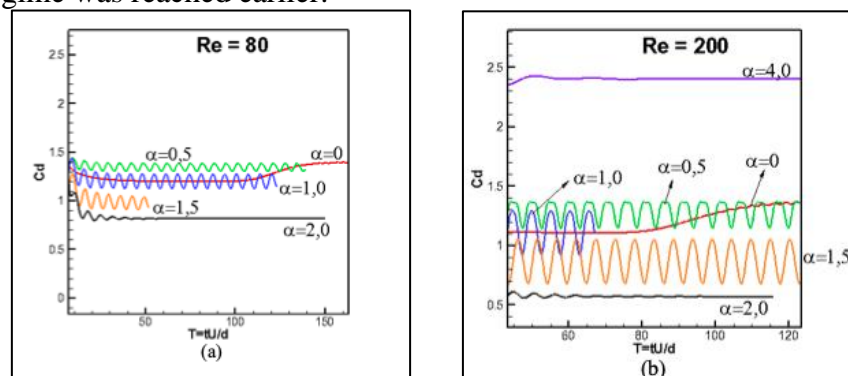


Figure 5.7 – Temporal evolution of the drag coefficient for (a) $Re = 80$ and (b) $Re = 200$ for different values of α .

Furthermore, with rotation the oscillations of the Cd are larger to the point where the vortices are inhibited, where they disappear. The higher the Reynolds number, the greater the Cd oscillations

and therefore, the greater the critical α value necessary to completely inhibit the process of generation and detachment of vortices. A single simulation with $\alpha = 4.0$ and $Re = 200$ was performed and it was observed that a significant increase in drag occurred.

The Fig. 5.8 shows that for this value of $\alpha = 4.0$ the velocity field close to the cylinder is greatly affected. There is a region where the fluid recirculates around the cylinder, increasing the contribution of the drag force. Further investigations in this rotation range for other Reynolds numbers should be carried out.

In the following figure, the simulation of the evolution of the lift coefficient as a function of dimensionless time is presented, for different Reynolds numbers and different specific rotations.

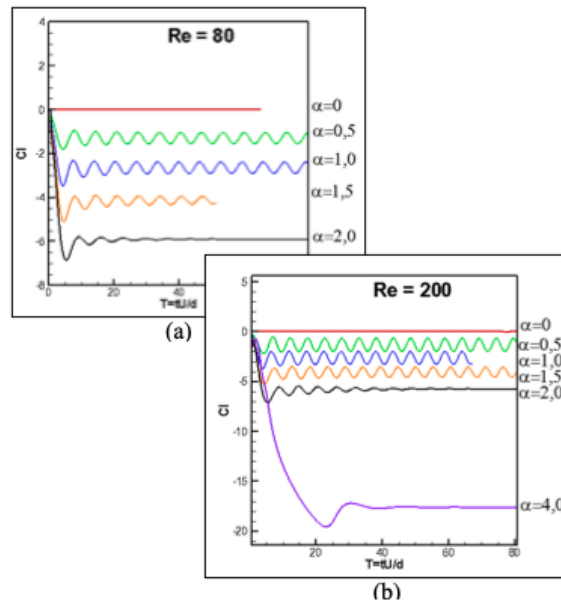


Figure 5.8 – Temporal evolution of the lift coefficient for (a) $Re = 80$ and $Re = 200$, for different values of α .

It is possible to clearly observe the increase in the lift coefficient with the increase in α . For the stationary case, Cl fluctuations also exist and increase with increasing Re , but the scale adopted in Fig. 5.8 does not allow Cl variations at $\alpha = 0$ to be visualized. For the lowest Reynolds values ($Re = 80$) these oscillations are intermittent and of low frequency. The Cl oscillations increase with $\alpha \leq \alpha_{critical}$ and also with the Reynolds number, however, the average values of the lift coefficient Cl are the same for a given value of α .

The Figure 5.9 shows the temporal evolution of the number of Nu for all simulated cases. For the stationary cylinder, the Nusselt number is maximum at the point $\theta = 0^\circ$, in front of the cylinder, and minimum at the back at $\theta = 180^\circ$. The rotation effect caused the symmetry shown in the $\alpha = 0$ curves to be lost. As α increases, the minimum point is displaced in the direction of rotation. It is also observed that the maximum Nusselt variation tends to increase with the increase in the Reynolds number. The temporal evolution of the Nusselt number is presented in Fig. 5.9.

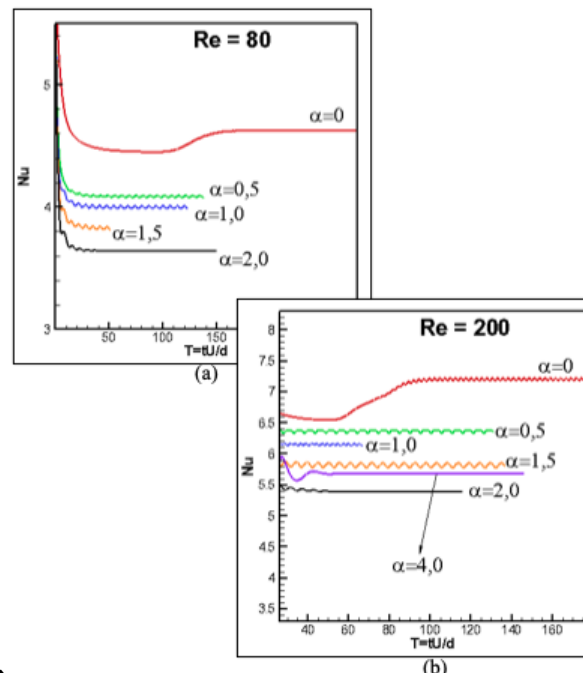


Figure 5.9 - Nusselt number around the cylinder for different Re and different α .

It is observed that the curves are similar to those of the drag coefficient, however, the increase in Nusselt is more pronounced with the increase in α . The Nusselt number is strongly influenced by the flow dynamics.

The amplitudes of the oscillations are also increased with α , but to a lesser extent than those of the drag coefficient. Mean Nusselt values decreased with increasing α to values of $0 \leq \alpha \leq 2.0$. The rotational movement creates a region close to the cylinder where the fluid is trapped, preventing the cylinder from exchanging heat with the fluid in the free stream. This behavior was also verified in the works of Chou and Kalina (1982) and Badr and Dennis (1985). This zone of recirculating fluid is called the “buffer” zone and is responsible for restricting heat exchange with the colder fluid, causing the Nusselt value to decrease. For $Re = 200$ and $\alpha = 4.0$ there was an increase in Nusselt, when compared to $\alpha = 2.0$. For this rotation rate the recirculation zone behind the cylinder disappears, as can be seen in Fig. 5.6, however a greater influence of the free current on the cylinder is verified and is possibly the reason for the increase in Nu for $\alpha = 4.0$.

The following figure shows an instantaneous distribution for all simulated cases. For the stationary cylinder, the Nusselt number is maximum at the point $\theta \cong 0^\circ$ at the front of the cylinder and minimum at the back at $\theta \cong 180^\circ$, proving that the temperature is minimum and maximum at these points. With the increase in the number of Re , the number of Nu starts to present two minimum points, close to $\theta \cong 150^\circ$ and $\theta \cong 250^\circ$, in the rear part of the cylinder. In these regions there are fluid recirculation bubbles that form and break away all the time. The rotation effect caused the symmetry shown in the $\alpha = 0$ curves to be lost. It is also observed that the maximum Nusselt variation tends to increase with the increase in the Reynolds number.

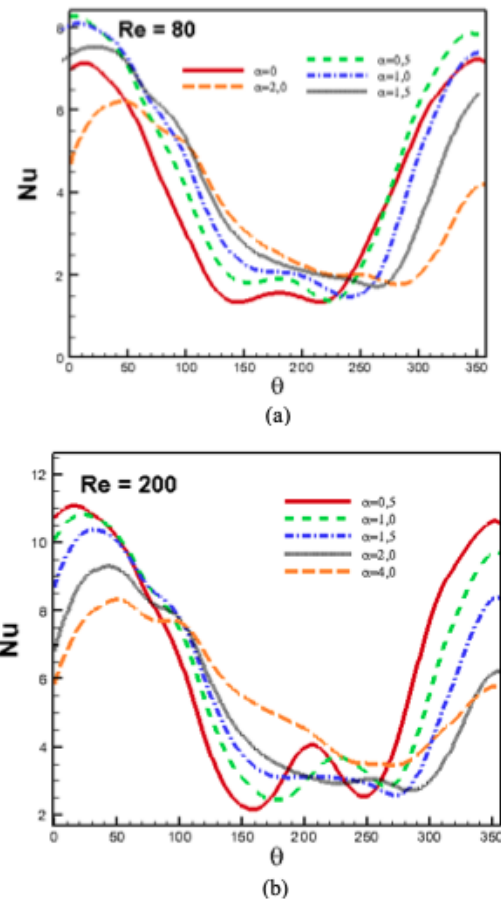


Figure 5.10 – Comparison of the local Nusselt number distribution over the cylinder surface for different Reynolds numbers and different values of α .

In Fig. 5.11, which represents the relationship between the lift coefficient as a function of the specific rotation and the Reynolds number, the polynomial function used for the average value of the lift coefficient was $\bar{C}_\ell = 0,7105\alpha^2 + 1,497\alpha + 0,2122$ for $0 < \alpha < 4,0$, also obtaining a proportional increase in the lift coefficient, in the present work resulting in $\bar{C}_\ell = 2,7092\alpha$, compared to the increase relationship given by Kang *et al.* (1999) which went from $\bar{C}_\ell = 2,475\alpha$ to $0 < \alpha < 2,0$. Resulting in a numerical agreement.

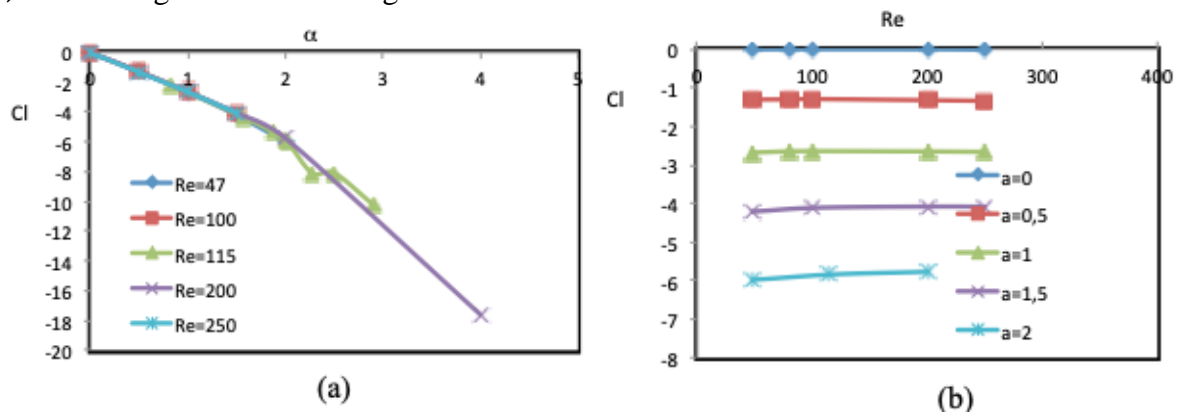


Figure 5.11 – Lift coefficient as a function of different values of α and Reynolds, (a) and (b).

It can be observed that despite the differences found between the C_d and C_l values, compared to Kang *et al.* (1999), both data sets show the same trend. In fact, in both cases, with the increase in specific rotation, the lift coefficient increases continuously, providing, at the same time, a drop in the drag coefficient.

6. Conclusions

Flow phenomena over circular cylinders, with or without heating, and with or without rotational movement, hold significant potential for various applications, notably in engineering. However, these potential applications remain largely unexplored. Such flows offer opportunities for devices capable of achieving high lift coefficients and for the active control of flow boundary layers. The methodology employed in this study is rooted in the conservation equations of momentum, mass, and energy, which describe the physics of practical flows.

This research builds upon previous work by Santos (2014), aiming to advance the application of this methodology to flow problems over heated obstacles subject to forced convection. A computational code was developed in C/C++ to simulate flows around stationary and rotating circular cylinders with heating. The obtained results include the vorticity field, temperature distribution, and various flow parameters such as average drag, lift, pressure coefficients, Strouhal, and Nusselt numbers. These results were compared with experimental and numerical data to validate the methodology for moving boundary problems and to assess the effect of forced convection heat transfer at Reynolds numbers below 250.

The existing literature on this subject is limited, with most studies focusing solely on drag and lift coefficients. Few studies investigate thermal effects alongside the behavior of Strouhal and Nusselt numbers as functions of Reynolds number (Re) and specific rotation (α). A deeper understanding of the flow characteristics around heated rotating cylinders could unveil practical applications.

This study employs a two-dimensional thermofluid dynamic analysis to comprehensively explore the flow phenomena. It evaluates the thermal impact of the cylinder on the flow, the generation of vortices, and the dynamics of Von Kármán wake formation and suppression across a range of Reynolds numbers ($80 \leq Re \leq 250$) and specific rotations ($0 < \alpha < 4.0$). The influence of rotation on reducing drag and increasing lift is observed, alongside the distribution of the thermal field near the cylinder. The temporal evolution of drag and lift coefficients, vortex shedding frequency (Strouhal number), and Nusselt number are analyzed.

With rotational movement, the vortex wake is displaced relative to the horizontal flow line, a displacement that increases with higher specific rotation values. As rotation increases, the oscillation amplitude of fluid dynamic coefficients tends toward zero, indicating a reduction in vortex generation. Conversely, average drag coefficients decrease while lift coefficients increase with rotation. Additionally, it is noted that the Strouhal number exhibits little influence at low specific rotation values but is dependent on Reynolds number. Quantitative results demonstrate good numerical agreement with findings in the literature.

Acknowledgements

The authors express their sincere gratitude to the esteemed editorial team of the *The Journal of Engineering and Exact Sciences - (JCEC)* for their tireless dedication and steadfast commitment to academic excellence. The rigorous peer review process and continual support provided have significantly enhanced the quality and impact of our research. We deeply value the meticulous care and attention invested in every phase of the editorial journey. This study owes its realization to the invaluable guidance and support from *JCEC*. Additionally, co-author acknowledges the support from CNPq 304271/2021-7.

Authors Contribution

Rômulo D. C. Santos: Conceptualization, Methodology, Development of Computational Code, validation, formal analysis, investigation, resources, writing, original, draft preparation, writing, review and editing, visualization. **Jorge H. O. Sales:** Writing, review and editing.

References

- Badr, H. M., & Dennis, S. C. R. (1985). Laminar forced convection from a rotating cylinder. *International Journal of Heat and Mass Transfer*, 28(1), 253-264. [https://doi.org/10.1016/0017-9310\(85\)90027-4](https://doi.org/10.1016/0017-9310(85)90027-4)
- Baranyi, L. (2003). Computation of unsteady momentum and heat transfer from a fixed circular cylinder in laminar flow. *Journal of computational and applied Mechanics*, 4(1), 13-25. <https://real.mtak.hu/6772/>
- Carvalho, G. B. D. (2003). Estudo experimental do escoamento em torno de cilindros circulares em movimento de rotação. *Masters dissertation*. São Paulo State University, Ilha Solteira, São Paulo, 2003. <https://repositorio.unesp.br/server/api/core/bitstreams/7c22d689-8ef8-4371-916b-1f67083d839f/content>
- Chorin, A. J. (1968). Numerical solution of the Navier-Stokes equations. *Mathematics of computation*, 22(104), 745-762.
- Chou, D. C., & Kalina, J. A. (1982). Heat transfer characteristics and boundary layer development about heating and cooling rotating blunt bodies at supersonic speeds. In *International Heat Transfer Conference Digital Library*. Begel House Inc.. [10.1615/IHTC7.1610](https://doi.org/10.1615/IHTC7.1610)
- Elghnam, R. I. (2014). Experimental and numerical investigation of heat transfer from a heated horizontal cylinder rotating in still air around its axis. *Ain Shams Engineering Journal*, 5(1), 177-185. <https://doi.org/10.1016/j.asej.2013.09.008>
- Goldstein, D., Handler, R., & Sirovich, L. (1995). Direct numerical simulation of turbulent flow over a modeled riblet covered surface. *Journal of Fluid Mechanics*, 302, 333-376. <https://doi.org/10.1017/S0022112095004125>
- Hughes, W., Bighthon, J., & Winowich, N. (1999). *Shaum's Outline of Fluid Dynamics*. *Schaum's Outline Series*. McGraw-Hill Companies, Incorporated.
- Incropera, F. P., Dewitt, D. P., & Bergman, T. L. (2000). *Fundamentos de Transferência de Calor e de Massa*. Grupo Gen-LTC.
- Kang, S., Choi, H., & Lee, S. (1999). Laminar flow past a rotating circular cylinder. *Physics of Fluids*, 11(11), 3312-3321. <https://doi.org/10.1063/1.870190>
- Kim, J., & Moin, P. (1985). Application of a fractional-step method to incompressible Navier-Stokes equations. *Journal of computational physics*, 59(2), 308-323. [https://doi.org/10.1016/0021-9991\(85\)90148-2](https://doi.org/10.1016/0021-9991(85)90148-2)
- Liu, H. R., & Ding, H. (2015). A diffuse-interface immersed-boundary method for two-dimensional simulation of flows with moving contact lines on curved substrates. *Journal of Computational Physics*, 294, 484-502. <https://doi.org/10.1016/j.jcp.2015.03.059>
- Mahir, N., & Altaç, Z. (2008). Numerical investigation of convective heat transfer in unsteady flow past two cylinders in tandem arrangements. *International Journal of Heat and Fluid Flow*, 29(5), 1309-1318. <https://doi.org/10.1016/j.ijheatfluidflow.2008.05.001>
- Page, L. G., Bello-Ochende, T., & Meyer, J. P. (2011). Maximum heat transfer density rate enhancement from cylinders rotating in natural convection. *International Communications in Heat and Mass Transfer*, 38(10), 1354-1359. <https://doi.org/10.1016/j.icheatmasstransfer.2011.08.010>
- Paramane, S. B., & Sharma, A. (2009). Numerical investigation of heat and fluid flow across a rotating circular cylinder maintained at constant temperature in 2-D laminar flow regime. *International Journal of Heat and Mass Transfer*, 52(13-14), 3205-3216. <https://doi.org/10.1016/j.ijheatmasstransfer.2008.12.031>

- Peskin, C. S. (1977). Numerical analysis of blood flow in the heart. *Journal of Computational Physics*, 25(3), 220-252. [https://doi.org/10.1016/0021-9991\(77\)90100-0](https://doi.org/10.1016/0021-9991(77)90100-0)
- Peskin, C. S., & McQueen, D. M. (1995, January). A general method for the computer simulation of biological systems interacting with fluids. In *Symposia of the society for Experimental Biology* (Vol. 49, pp. 265-276).
- Ren, W., Shu, C., & Yang, W. (2013). An efficient immersed boundary method for thermal flow problems with heat flux boundary conditions. *International Journal of Heat and Mass Transfer*, 64, 694-705. <https://doi.org/10.1016/j.ijheatmasstransfer.2013.05.020>
- SANTOS, R. D. C. D. (2014). Análise Bidimensional Termo-Fluido Dinâmica de Cilindros Rotativos com o Método da Fronteira Imersa/Modelo Físico Virtual. *Masters' dissertation*. Federal University of Itajubá, Minas Gerais, 2014. <https://repositorio.unifei.edu.br/xmlui/handle/123456789/308>
- Santos, R. D. C. dos, & Sales, J. H. de O. (2023). Analysis and simulation of turbulent flow around an immersed body with constant temperature using the Immersed Boundary Method. *The Journal of Engineering and Exact Sciences*, 9(11), 16664–01e. <https://doi.org/10.18540/jcecvl9iss11pp16664-01e>
- Schneider, G. E., & Zedan, M. (1981). A modified strongly implicit procedure for the numerical solution of field problems. *Numerical Heat Transfer*, 4(1), 1-19. <https://doi.org/10.1080/01495728108961775>
- Sharma, V., & Dhiman, K. A. (2012). Heat transfer from a rotating circular cylinder in the steady regime: Effects of Prandtl number. *Thermal Science*, 16(1), 79-91. <https://doi.org/10.2298/TSCI100914057S>
- SHRIVASTAVA, V., BADAMI, P., Hiremath, N., SARAVANAN, V., & SEETHARAMU, K. (2012). Numerical investigation of heat transfer for flow around circular cylinder with triangular and rectangular wake splitter. *Word Academy of Science, Engineering and Technology*, (69), 406-416.
- Silva, A. L. E., Silveira-Neto, A., & Damasceno, J. J. R. (2003). Numerical simulation of two-dimensional flows over a circular cylinder using the immersed boundary method. *Journal of Computational Physics*, 189(2), 351-370. [https://doi.org/10.1016/S0021-9991\(03\)00214-6](https://doi.org/10.1016/S0021-9991(03)00214-6)
- Unverdi, S. O., & Tryggvason, G. (1992). A front-tracking method for viscous, incompressible, multi-fluid flows. *Journal of computational physics*, 100(1), 25-37. [https://doi.org/10.1016/0021-9991\(92\)90307-K](https://doi.org/10.1016/0021-9991(92)90307-K)
- Vedovoto, J. M. (2007). Modelagem matemática e simulação numérica de escoamentos incompressíveis sobre geometrias complexas tridimensionais utilizando o método da fronteira imersa. *Doctoral thesis*. Federal University of Uberlândia, Minas Gerais, 2007. <https://repositorio.ufu.br/handle/123456789/15023>
- Ye, T., Mittal, R., Udaykumar, H. S., & Shyy, W. (1999). An accurate Cartesian grid method for viscous incompressible flows with complex immersed boundaries. *Journal of computational physics*, 156(2), 209-240. <https://doi.org/10.1006/jcph.1999.6356>